A laboratory-scale binder jet additive manufacturing testbed for process exploration and material development

A laboratory-scale binder jet additive manufacturing testbed for process exploration and material development

Cite this article as: Daniel Oropeza, A. John Hart, A laboratory-scale binder jet additive manufacturing testbed for process exploration and material development, *The International Journal of Advanced Manufacturing Technology*, doi: 10.1007/s00170-021-07123-1

Title: A laboratory-scale binder jet additive manufacturing testbed for process exploration and material development

Authors: Daniel Oropeza[1] and A. John Hart[1]

Corresponding Authors: D. Oropeza (dan.oropeza@gmail.com), A.J. Hart (ajhart@mit.edu)

Affiliations:

1. Department of Mechanical Engineering, Massachusetts Institute of Technology, Cambridge, MA 02139 USA.

Abstract

Binder jet additive manufacturing (BJAM) is capable of fabricating complex three-dimensional components from a variety of material classes. Understanding the fundamentals of BJAM, including spreading of thin layers of powder, powder-binder interactions, and post-processing is critical to develop robust process parameters for BJAM. Toward meeting these needs, this work presents the design, fabrication, and qualification of a testbed for modular, mechanized, BJAM. The testbed seeks replicate the operating conditions of commercial AM equipment and features fully programmable motion control including powder spreading using a precision roller mechanism, powder supply via a vibrating hopper, and gantry positioning of an inkjet printhead. The inkjet deposition system allows for the use of variable nozzle diameters, the exploration of novel binder compositions, and full control of jetting parameters. Validation of the accuracy and repeatability of the machine and its subsystems, as well as the fabrication of exemplary stainless steel components, are described. The precision engineered testbed can therefore enable the study of the BJAM process, exploration of novel binder compositions, and processing of custom powders to further scientific research and industrial applicability of BJAM.

Keywords

Additive manufacturing, binder jetting, inkjet printing, precision machine design

Declarations

Funding

This work was supported by a NASA Space Technology Research Fellowship to D.O. Additional financial support for hardware and experiments was provided by a grant from Lockheed Martin Corporation.

Conflict of interest/Competing interest

Not applicable.

Availability of data and material

Data available upon reasonable request from the authors.

Code availability

Not applicable.

Author contributions: CRediT taxonomy

Daniel Oropeza: Conceptualization, Methodology, Software, Validation, Formal analysis, Investigation, Resources, Data curation, Writing – original draft preparation, Writing – review and editing, Visualization, Supervision, Project administration, Funding acquisition. **A. John Hart:** Conceptualization, Methodology, Writing – reviewing and editing, Funding acquisition.

Ethics approval

Not applicable.

Consent to participate

Not applicable.

Consent to publication

Not applicable.

Acknowledgements

This work was supported by a NASA Space Technology Research Fellowship to D.O. Additional financial support for hardware and experiments was provided by a grant from Lockheed Martin Corporation. The authors thank the MIT Institute for Soldier Nanotechnologies and Reed A. Kopp for access to and assistance with the micro-CT scanner.

1. Introduction

Binder jet additive manufacturing (BJAM), initially named Three Dimensional Printing (3DP) upon its inception at MIT by Sachs, Cima et al. [1–4] operates by layer-wise inkjet deposition of a binder onto a powder bed, followed by optional consolidation to a dense component. BJAM is a highly attractive additive manufacturing (AM) process due to its compatibility with virtually any powder material, high build rate compared to other AM methods, capability for high resolution, and scalability to very large build volumes (e.g., 100s mm length) [4,5]. A further attribute of BJAM is that the materials remain in the solid state throughout the process, and the geometrical shaping of the part is decoupled from the thermal densification step. This enables some degree of microstructural control during sintering, but presents challenges in maintaining shape accuracy due to shrinkage and warping [4,5].

More specifically, BJAM follows four steps to produce finished parts: (1) powder layer deposition and spreading, (2) binder delivery via inkjet deposition, with steps (1) and (2) repeated until the desired 3D geometry is completed, (3) removal of the green (i.e., binder-bound or printed) part from powder bed with optional binder curing prior to part removal, (4) post-processing of the green part (e.g., debinding, sintering, infiltration), followed by optional post-processing (e.g., sand blasting, polishing, coating). Thus, the two mechanisms for material delivery in BJAM are powder spreading and inkjet deposition, and these mechanisms are responsible for the part geometry and green density that ultimately affect final part properties. Figure 1 shows a conceptual image of the binder jetting process with possible variations of spreading tool geometries (i.e., stiff or compliant blade, roller) and compaction strategies for powder spreading, as well as the powder-binder interactions that occur through the inkjet binder deposition process.

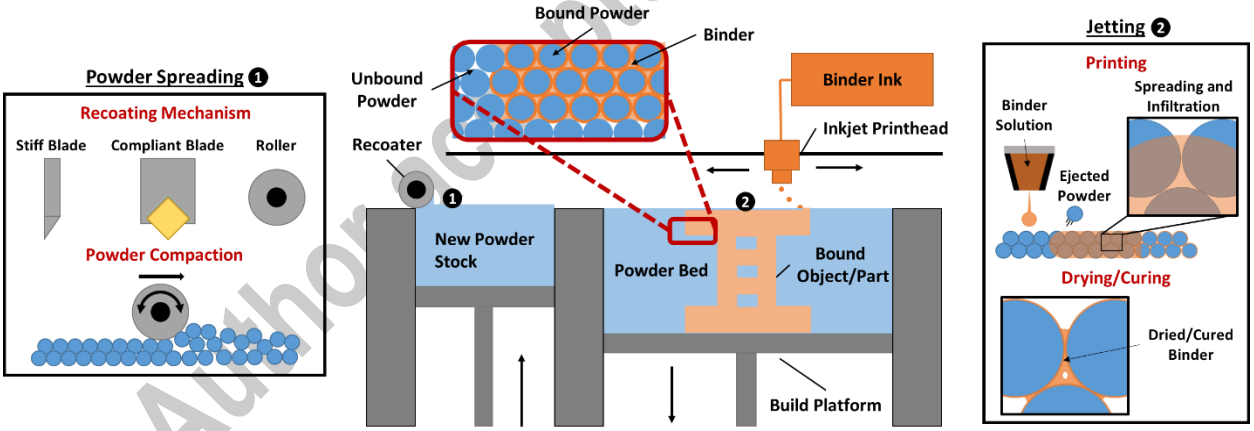

Figure 1 – Conceptual image of binder jet additive manufacturing highlighting (1) powder spreading variations and (2) powder-binder interactions during jetting.

For extensive reviews on prior work for BJAM, the reader is directed to review articles by Mostafei et al. [6], Ziaee and Crane [5], and Mirzababei and Pasebani [7]. Briefly, BJAM is compatible with stainless steels [7,8], titanium alloys [9], Inconel [10–12], tungsten alloys [13], copper [14], sand [15,16], alumina ceramics [17,18], carbide ceramics [19–21], magnetic alloys [22], and many other materials. Commonly, BJAM produces components with green (as-printed) density between 40-60% [5–7]. Challenges for BJAM process development stem from the need to form uniform, high-density powder layers and the deposition of appropriate binder to provide green strength and enable post-processing (e.g., infiltration,

sintering) to attain the desired geometry, microstructure and properties [4–6,23]. Defects introduced during BJAM are exacerbated during post-processing (e.g., sintering) and result in strength-limiting flaws and geometric distortion [5,6,23]. The favorable inverse relationship between sintering rate and powder size [23], and the diversity of materials compatible with BJAM, suggests that the ability to optimize powder spreading, binder development, powder-binder interactions, and post-process densification can result in impactful advances for the BJAM process.

Exploration of processing parameters for powder spreading and inkjet deposition for BJAM has led to key insights on the use of multi-modal and fine powders as feedstocks [10,11,24,25], the use of roller mechanisms and vibration in the recoating process [26–30], and the influence of powder-binder interactions on print quality [3,18,31–33]. Although the use of finer powder sizes results in increased sintering rates during BJAM post-processing, powders with average size <20 μm tend to result in agglomeration during spreading due to strong cohesive forces [23,34–36]. Using non-spherical particle shapes compromises powder spreadability and packing density, but reduces particle ejection during ballistic impact from inkjet droplets due to higher interparticle friction [31,34]. Therefore, when fine or irregular powder particles are used in BJAM, and in powder bed AM overall, a shear force must be applied (usually via a counter-rotating roller) to break powder agglomerates and improve spreadability and packing density. The use of powders with a tailored multi-modal size distribution has been proven to increase the green density of a powder compact, however the multi-modal distribution can result in non-homogenous sintering conditions and limited gain in densification if powder size distributions are not optimized for sintering [23,24,34,35]. Optimization of powder spreading, via spreading mechanism design and roller motion is key to forming a dense powder bed [10,26–28]. Additionally, vibration of the spreading mechanism or powder bed can result in increased powder bed densities, but can have the adverse effect of disturbing the printed part [28,37].

Jetting parameters such as droplet velocity, droplet spacing, droplet frequency, and binder saturation must be characterized and optimized for any chosen binder system to produce high density green parts [19,31–33]. Additionally, the interactions which govern powder-binder wetting and infiltration, binder primitive formation, and powder particle ejection are unique to each powder-binder combination [3,31–33,38–42]. Polymer binders are commonly used in BJAM as they bind most materials and can decompose to leave little organic residue [43–45]. However, the polymer is not an active participant in the densification of the printed component, requiring a debinding step that can result in part warping and deformation [46–49]. To prevent part warping and improve densification, nanoparticle additives have been used either as a post-process addition or for a limited range of materials [17,46,47,50–56].

Although commercial BJAM equipment has been available for >20 years, recent interest in industrialization of BJAM has resulted in increased research and commercial activity [4–6]. Other AM methods (e.g., extrusion-based, powder bed fusion) have benefited not only from the development of commercial equipment, but also precision testbeds capable of exploring AM process fundamentals [57–64]. For powder bed fusion (PBF), testbeds to explore powder spreading, laser-powder interactions, and in-process metrology and control [57,58,65,66] have advanced fundamental understanding of the process and accelerated the development of process standards. For BJAM, further understanding of powder spreading and powder-binder interactions, exploration of low-cost fine powders (e.g., based on metal injection molding feedstock), and development of new binding agents, will further industrialization.

No standard equipment exists for characterization of powder spreading or inkjet deposition for BJAM, although various studies have utilized ExOne or similar commercial printers [8–12,14,18–22,24–26,29,46,47,52,67,68]. For reference, the ExOne Innovent+ printer is capable of a build volume of 160 mm x 65 mm x 65 mm, layer thicknesses between 30-200 µm, and nozzle diameters available between ~10 and ~30 µm (10-80 pL volumes) for a minimum voxel size of 30 µm [69]. Further, reported recoating (spreading) lateral speeds are 10-130 mm/s, and when a roller is used the rotation rate is typically 250-350 RPM [6,8–11,11,18–20,22,24,70]. Although some open-source hobby/maker designs exist for BJAM (e.g., Oasis 3DP, Plan B), the precision of these printers has not been qualified and the use of a thermal printhead places limitations on the fluids that can be dispensed and results in heat-induced kogation (i.e., deposition of residue from ink decomposition). Therefore, the majority of industrial BJAM printers use piezoelectric inkjet printheads [71–73]. Moreover, exploration of novel powder feedstock materials produced at small quantities (<100 g) and novel binders at small volumes (<10 mL) provide great benefit through rapid and cost-effective parameter development and component prototyping via BJAM. Yet, the exploration of novel binders is limited by issues such as printhead loading, clogging, and cleaning, as well as maintaining solvent compatibility for printhead ink and cleaning solutions; early stage process development is thus difficult using commercial equipment with industrial inkjet printheads [50,51,67,68].

Here, we present the design and fabrication of a precision BJAM testbed suited to the investigation of process fundamentals, parameter development, and novel materials in small quantities. Our testbed is modular and enables fabrication of multi-layer components, and therefore can facilitate correlation among powder and binder characteristics, process parameters (e.g., spreading parameters, layer height, jetting parameters), and green part properties. Compared to commercial AM equipment, the testbed allows for experimentation with smaller quantities of powders and binders, as well as fully programmed control of the spreading device, powder supply mechanism, and build platform. The testbed's functionality is demonstrated via printing and characterization of exemplary green parts using stainless steel powder and a polymer binder.

2. Design and construction of the binder jetting testbed

2.1 Overview of system and capabilities

The BJAM testbed fits on a tabletop (500 mm x 500 mm x 400 mm) and is the combination of a powder spreading testbed (previously fabricated and described by Oropeza et al. [74]) and an inkjet printing testbed, which are mechanically and electrically integrated to enable programmed binder jetting. Figure 2 shows the CAD model and fabricated apparatus, as well as images taken during a binder jetting experiment. During operation of the BJAM testbed, powder is supplied to the spreading mechanism (e.g., roller, blade) via the powder supply piston or a powder hopper, the powder is spread over the build platform (which controls layer thickness), inkjet deposition occurs over the build platform, and then binder drying and/or curing is performed with the integrated heat lamp (Online Resource 1). For spreading, the user can choose the spreading tool geometry, spreading translation speed and rotation, layer height, and optional post-print compaction. Control over the inkjet nozzle diameter, inkjet droplet frequency, inkjet droplet velocity, printhead traverse velocity, jetting position, and heating time, as well as control over the spreader mechanism, spreading translation speed and rotation, layer height, and compaction are all possible with the custom testbed.

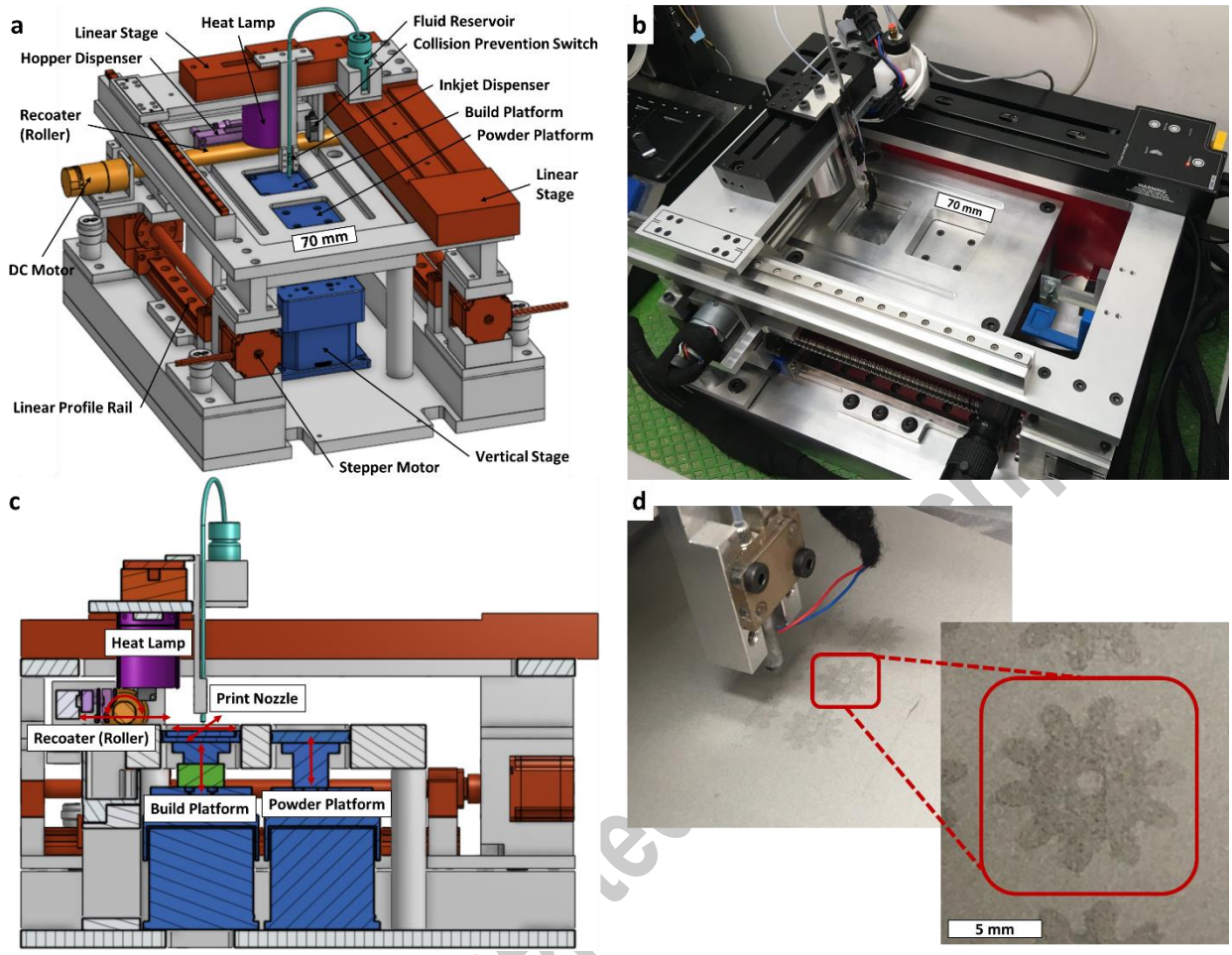

Figure 2 – Binder jetting testbed: (a) CAD model showcasing major components with roller installed as the powder spreading tool; (b) fabricated binder jetting testbed; (c) sectional side-view highlighting moving components and trajectories; (d) images from binder jetting experiment using stainless steel 316L 15-45 µm powder and polymer binder, printing an array of gear geometries on the build platform.

The testbed was designed according to the target specifications listed in Table 1, and is suited for processing custom powder feedstocks (e.g., polymer, metal and ceramic powders) and binder compositions (e.g., polymer, nanoparticle suspensions, metal salt solutions). The following are the major modules of the machine, including a summary of the modules for powder spreading testbed (denoted by * below) described by Oropeza et al. [74]:

Powder supply platform*: Powder is supplied using a vertical platform (travel distance of 20 mm), consisting of a motorized axis and a custom-machined pillar and piston.

Modular powder spreading mechanism*: A custom-designed linear motion system is used to translate the powder spreading mechanism. The spreading mechanism has mounting features that allow the interchange of different spreading tools (e.g., motorized roller, stiff blade, compliant blade). For the BJAM experiments described here, a precision roller is used to spread powder from the powder supply platform and onto the build platform. A hopper dispensing system may alternatively be used for direct deposition of powder on the build platform, followed by spreading using the motorized tool.

Build platform*: The build platform presents the surface onto which the part is built. The build platform has a removable build plate and an integrated load cell, which can be used to measure powder compaction forces. These components are attached to a motorized (vertical) axis via a custom-machined pillar and piston. The build platform has a vertical travel distance of 20 mm, is capable of measuring loads up to 100 N, and the build (spreading) area is 60 mm x 60 mm.

Inkjet deposition system: An X-Y gantry motion system coupled with a piezoelectric inkjet dispensing system enable precise deposition of <100 µm droplets over the build area. Additionally, a heat lamp mounted on the inkjet motion system assists drying and curing of the binder after deposition.

Vision system: A video camera is focused at the inkjet nozzle home location and along with a controllable strobe LED, assist in setting and validating ink jetting parameters.

Control software: A custom LabView program controls all system operations and allows for specification of all process parameters.

Table 1 – Summary of desired design specifications for binder jetting testbed, including specifications for powder spreading testbed.

Parameter	Design Values
Spreader Type	Interchangeable; roller or blade
Powder Dispensing Mechanism	Piston and/or hopper
Spreading Tool Traverse Speed	0-100 mm/s
Roller Rotation	0-300 rpm
Build Platform Minimum Incremental Motion	5 µm (vertical)
Dispenser Nozzle Diameter	Modular; 20-80 µm*
Jetting Frequency	< 1 kHz*
Binder Viscosity	< 20 cPs*
Binder Surface Tension	20-70 dynes/cm*
Minimum Binder Reservoir Volume	10 mL
Build Volume	60 x 60 x 20 mm (LxWxH)
Machine Volume	450 x 500 x 400 mm (LxWxH)

*Specifications of MicroFab Dispensing System

2.2 Detailed description of testbed modules

Here we detail the inkjet module which consists of an inkjet dispenser mounted on single-axis linear motion systems stacked in an X-Y configuration. The module is kinematically mounted on top of the powder spreading testbed; the modules and validation of the powder spreading apparatus have been previously presented in detail [74], and therefore are not described further in this paper.

2.2.1 Linear motion system: long-direction (Y-axis) and short-direction (X-axis)

The long-direction of motion (Y-axis) controls the position of the inkjet dispenser in the non-jetting direction, ultimately setting the line spacing during BJAM. The linear stage for the Y-axis (Thorlabs LTS300/M) provides a maximum travel velocity of 50 mm/s with listed repeatability of 2 µm and accuracy of 5 µm. The Y-axis motion system includes an integrated controller to drive the stepper motor. The short-direction of motion (X-axis) controls the position and velocity of the inkjet dispenser in the jetting direction. The linear stage for the X-axis of motion, or jetting direction, (Thorlabs DDSM100/M) provide a maximum 500 mm/s printhead traverse velocity with manufacturer-listed repeatability of 1.5 µm and accuracy of 5 µm. The X-axis linear stage is controlled using a brushless DC servo driver (Thorlabs KBD 101).

2.2.2 Inkjet droplet generation system

The jetting system consists of a piezoelectric drive controller (Microfab JetDrive V, CT-M5-01), a 20 mL fluid reservoir, gas and fluid tubing (LeeCo MINSTAC tubing), a single piezoelectric dispensing nozzle (Microfab MJ-AT-01-xxx, where xxx dictates the nozzle diameter), and a digital pressure controller (APEX Vacuum LLC). The diameter of the droplet can be varied by utilizing dispensing nozzles (available from 20-80 µm orifice diameter), the frequency of droplet ejection can be controlled up to 1 kHz, and the waveform sent to the piezoelectric dispenser can deliver up to 70V with dwell times up to 100s of µs. The pressure controller regulates the backpressure in the fluid reservoir and thus provides the appropriate static pressure at the nozzle tip for droplet ejection. The use of a single dispensing nozzle simplifies interchange of the binder system and reduces the time required to purge nozzle clogs which can occur when utilizing novel binders. Furthermore, the testbed was designed to be compatible with multi-nozzle inkjet printheads (e.g., Xaar 1201) that offer higher throughput for binder deposition.

2.2.3 Vision system

A custom optical setup allows imaging of droplets to determine suitable jetting parameters and ensure continuous jetting during binder jetting experiments. The setup comprises a USB CCD camera (Thorlabs High-Sensitivity USB 3.0 CMOS Camera), optics (Thorlabs 6.5X Zoom Lens with 3 mm Fine Focus, 0.50X Extension Tube, C-Mount Adapter, and 0.75X Magnifying Lens Attachments, with 6.28 µm resolving limit at high magnification), and a strobe LED (Microfab Technologies, Inc.). The strobe LED can be controlled to pulse at the same frequency as the piezoelectric actuator, with an additional pulse delay to capture droplets at different stages of jetting.

2.2.4 Heat lamp

As an optional drying and/or curing mechanism for the binder jetting process, a custom heat lamp system was constructed utilizing a halogen bulb (Sunlite ENH 250W Bulb, MR16 400W Socket), fully encapsulated and protected using a UV filter lens (WAC Lighting LENS-16-UVF) and a custom-machined aluminum casing. The power to the heat lamp is controlled using a microcontroller (Arudino Nano) and power relay (Digital Loggers IoT Relay). Use of the lamp to heat the powder bed can, for instance, assist in evaporation of binder solvent, or initiate polymerization or cross-linking of certain binders.

2.2.5 Collision prevention switch

To prevent potential damage to the inkjet system from errant contact with the recoating system, a switch which cuts power to machine was incorporated. The switch is mounted to the inkjet motion gantry and is triggered upon contact with the powder spreading system. The miniature push-button limit switch (McMaster Carr 7779K61) is connected to a microcontroller (Arudino Nano) and power relay (Digital Loggers IoT Relay) which controls the power to the testbed.

2.2.6 Software for binder jet testbed

Figure 3 schematically shows the electrical wiring and communications within the system. A custom LabView program was developed for control of all machine components, including concurrent control of the powder spreading testbed. For binder deposition onto the powder bed, synchronization of nozzle dispenser motion with triggering of the piezoelectric jetting system is critical. Therefore, the software controls the steps of each layer-wise cycle of BJAM which involves powder spreading, and controls the binder deposition process. A MATLAB script was written to convert user inputs (e.g., from a text file with part geometry generated via Autodesk Netfabb, jetting line spacing, nozzle diameter, etc.) to a text file which contains LabView-compatible machine commands. The text file is then used as an input to the LabView code which uses the control commands to drive the machine.

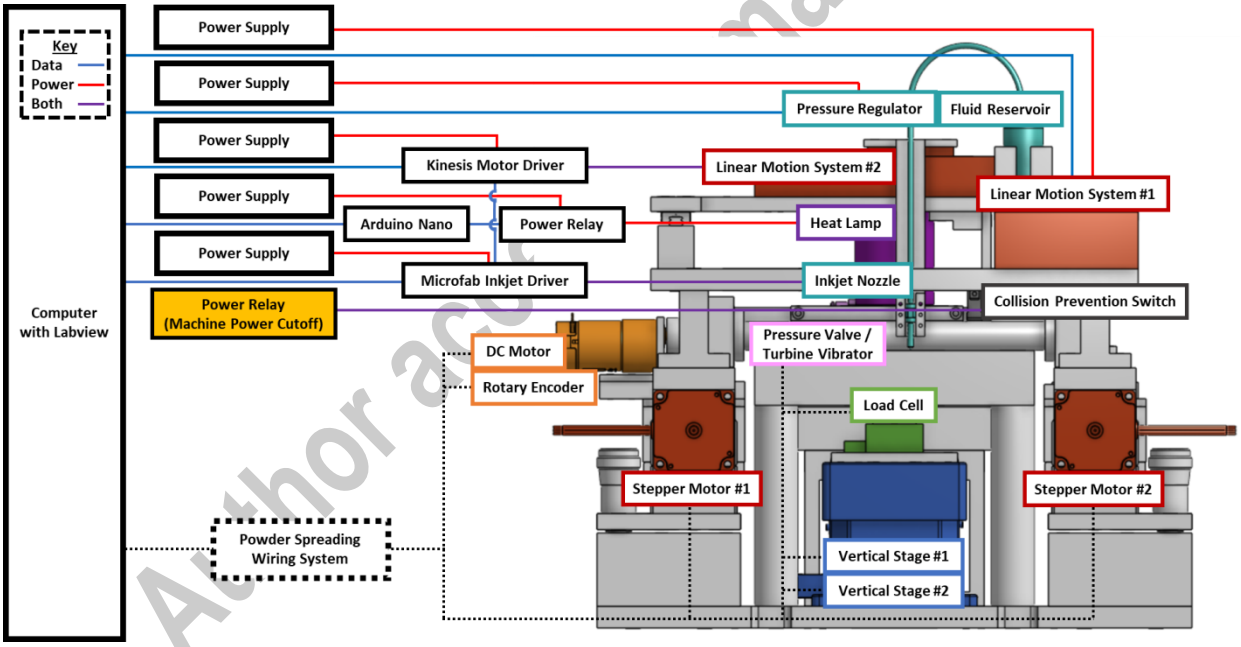

Figure 3 - Electronic connection diagram for binder jetting testbed, including abbreviated connections for powder spreading system.

3. Validation and experimentation

3.1 Binder jetting testbed validation

3.1.1 Linear motion system: traverse position

The resolution of the traverse motion of the inkjet nozzle in both the Y and X axes was measured using a laser point scanner (Keyence LK-G152, reported accuracy 0.5 µm). Measurements were performed by sending motion commands to a single axis with intervals ranging from 25 µm to 5 mm across the total range of -20 mm to +20 mm, with each condition being measured three times. As shown in Figure 4a, linear correlation for the Y-axis was demonstrated within ±50 µm, with repeatability within 30 µm (Figure S1a). Similarly, for the X-axis, linear correlation was demonstrated within ±30 µm as shown in Figure 4b, with repeatability within 5 µm (Figure S1b).

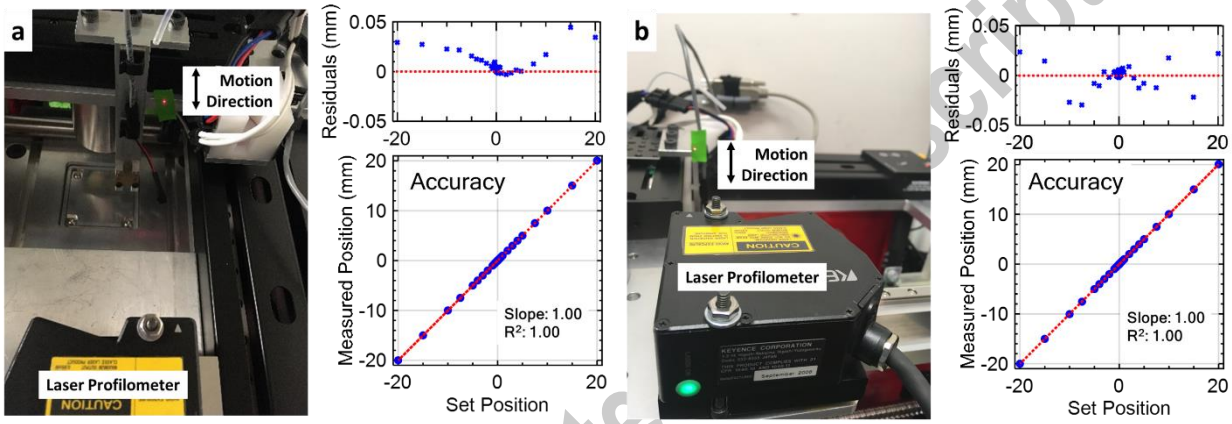

Figure 4 – Validation test setup, motion position accuracy and residuals to linear fit for (a) Y-axis and (b) X-axis (jetting direction).

3.1.2 Heat lamp: build area temperature profile

To estimate the energy deposition from the heat lamp over the build platform, the temperature above the build platform was measured using a thermometer (PerfectPrime TC2100) connected to a K-type thermocouple (McMaster Carr 6441T942). The measurement provides an estimate of the heating capabilities of the heat lamp and was performed by placing the thermocouple above the build platform (Figure S2a) and providing power to the heat bulb for a set amount of time. To estimate the heating profile at the center of the build platform, the heat lamp was turned on for 50 seconds, showcasing that the center of the build area reaches 100°C in 8 seconds and reaches 200°C in 48 seconds (Figure S2b) Furthermore, by varying the position of the thermocouple to nine positions over the build platform, we can estimate a heat profile for the build area after 30 seconds of energy deposition from the heat lamp over the build plate (Figure S2c).

To analyze the thermal conditions of a powder bed during an exemplary heating cycle, an infrared thermal camera (HTI HT-A2) was used to image the surface temperature of a 500 µm stainless steel powder layer (SS 316L, 15-45 µm, John Galt Steel). Powder was spread at a traverse speed of 50 mm/s without roller rotation at 55.5% humidity (AcuRite 01080M), in an ambient lab environment. Images were taken after 10 seconds, 30 seconds, and 60 seconds of heating. As shown in Figure 5, the central region (~40mm diameter) of the powder bed surface exceeds 80°C after 10 seconds and the region exceeds 100°C after 30 seconds of heating. This bed temperature of 100°C is sufficient to assist in drying

of common binder solvents (e.g., deionized water, 2-methoxyenthanol, ethanol), as well as being greater than the glass transition temperature for various polymers (e.g., polyethylene glycol, polyvinyl alcohol, polymethyl methacrylate), therefore showing the heating capability can assist in formation of a uniform binder film over powder particles [75]. The time-temperature dynamics attained by the powder bed will depend on the powder material (e.g., absorptivity), bed properties (e.g., packing density), and heat lamp parameters (e.g., bulb wattage, heating time), and should be calibrated for each experimental condition.

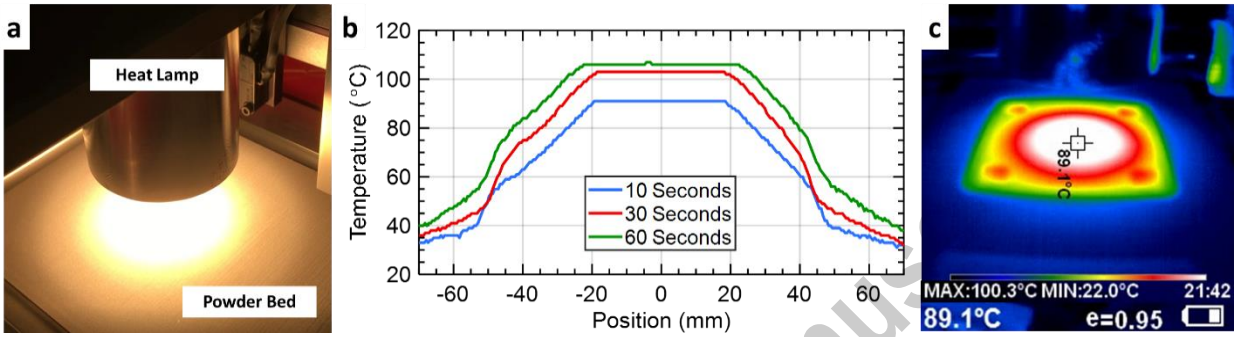

Figure 5 – (a) Validation test setup for thermal profile of powder bed after heating, (b) thermal profile over central region of build platform and (c) representative infrared image from experiments.

3.1.3 Vision system: droplet generation and imaging

To establish a stable jetting condition, the back pressure is set to the maximum value to purge the nozzle, then reduced until the meniscus is flush with the nozzle orifice. Once the pressure condition is set, the voltage and jetting time are adjusted until a droplet is generated by the system. To showcase the capabilities of the vision system, images of the inkjet dispensing nozzle and ejected droplets were taken using the custom optics system, shown in Figure 6. The outer diameter of the nozzle tip was determined to be 600.5 µm using a digital microscope (Zeiss Smartzoom 5). This value is used to set the scale for images taken using the vision system, and in turn to estimate the diameter and velocity of the ejected droplets. To estimate the diameter of ink droplets ejected from the 80 µm dispensing nozzle, a polyethylene glycol (PEG) binder (10% m/m PEG 6000 in DI water/ethanol, 20% mole ratio ethanol) was dispensed from the tip with a jetting voltage of 65 V and dwell time of 20 µs at 120 Hz jetting frequency. Ten different droplet images were captured at a 500 µs strobe delay and analyzed in Fiji/ImageJ to compute the droplet diameter from the droplet area estimated using the oval measurement tool, resulting in a droplet size of 81.0 ±1.4 µm. To estimate the droplet velocity, the same binder and jetting conditions were utilized, but sequential droplet images were taken at increasing strobe delays, resulting in capturing of the jetting sequence and droplet, shown in Figure 6b. The velocity was estimated using Fiji/ImageJ by dividing the change in droplet position by the change in strobe delay for the 350-750 µs images and averaged over five separate jetting sequences, resulting in a speed of 2.0 ±0.1 m/s.

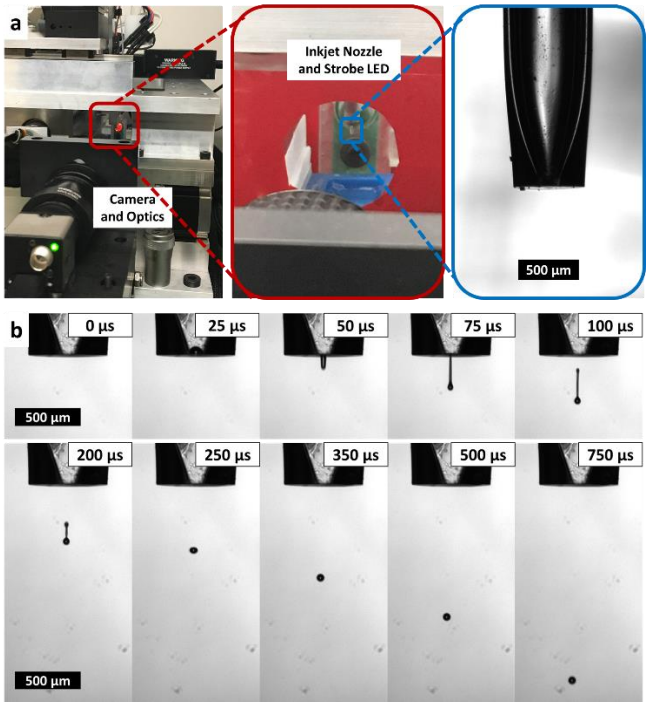

Figure 6 – (a) Vision system setup and (b) inkjet sequence of binder droplets using transparent (undyed) PEG binder.

3.1.4 Inkjet system: positional accuracy and drop spacing control for line formation

To showcase functionality and test the positional accuracy of the full inkjet module, a rectangle pattern of droplets (19 Y-axis x 21 X-axis) was deposited with a drop spacing and line spacing of 250 µm. To assist in imaging the droplets after deposition, the PEG binder was modified by adding 1% m/m black dye (Sigma Aldrich 211842) and the droplets were deposited on white copy paper (Xerox Business 4200) at a jetting traverse velocity of 25 mm/s, jetting voltage of 65 V, and jetting dwell time of 20 µs. A comparison between the MATLAB-generated droplet map and printed map is shown in Figure 7a. The deviation of each droplet position from its intended position was estimated using Fiji/ImageJ via the multi-point tool, showing a mean signed error of 4.9 ±20.5 µm and a mean absolute error of 17.3 ±12.1 µm for the droplet position in the X-axis (jetting direction) and a mean signed error of 15.5 ±10.8 µm and a mean absolute error of 5.5 ±18.1 µm for the droplet position in the Y-axis (non-jetting direction). These deviations are the result of compounding effects from the motion system, jetting anomalies at the nozzle tip during jetting, and wetting characteristics of the binder and substrate. Additionally, the size of the printed droplet was estimated using the particle analysis tool in Fiji/ImageJ as 187.9 ±5.5 µm or approximately 2.4X the droplet diameter. Thus, the droplet position deviation is an order of magnitude smaller than the critical dimension (i.e., diameter) of the droplet.

Additional patterns printed using the same dyed PEG binder and paper substrate, were used to evaluate the capability of the inkjet system to control droplet spacing and form continuous print lines, which is ultimately necessary to control binder saturation (i.e., the ratio of deposited binder volume to powder bed pore volume) and thereby ensure homogenous green strength and feature quality in the powder bed during BJAM. Droplet spacing ranging from 40 µm (i.e., 0.5X droplet diameter) to 250 µm was controlled by varying the jetting frequency from 625 Hz to 100 Hz (i.e., jetting traverse velocity was held constant at 25 mm/s), shown in Figure 7b. It was found that decreasing the droplet spacing below 120

µm (i.e., 1.5X droplet diameter) results in stable line formation throughout the print line for this setup. Fiji/ImageJ was used to estimate the line width, with an approximate line width of 368 µm for a 40 µm droplet spacing, 331 µm for 80 µm droplet spacing, and 295 µm for 120 µm droplet spacing. These line widths are only representative of the chosen binder and the paper test substrate, however, the formation of a stable line at nominal spacing of ≤0.5X droplet diameter is consistent with prior work on selection of droplet spacing for BJAM [17,32] and therefore this condition was utilized for binder jetting experiments that follow. Despite the obvious difference between the substrate-binder interactions (e.g., binder permeability and infiltration, particle displacement and ejection, substrate surface properties) of printing on paper versus a powder bed, the use of a monolithic porous substrate can serve as an initial screening tool. In the future, experiments could be performed to enable direct correlation of drop spreading on a model porous substrate to the behavior on the powder bed.

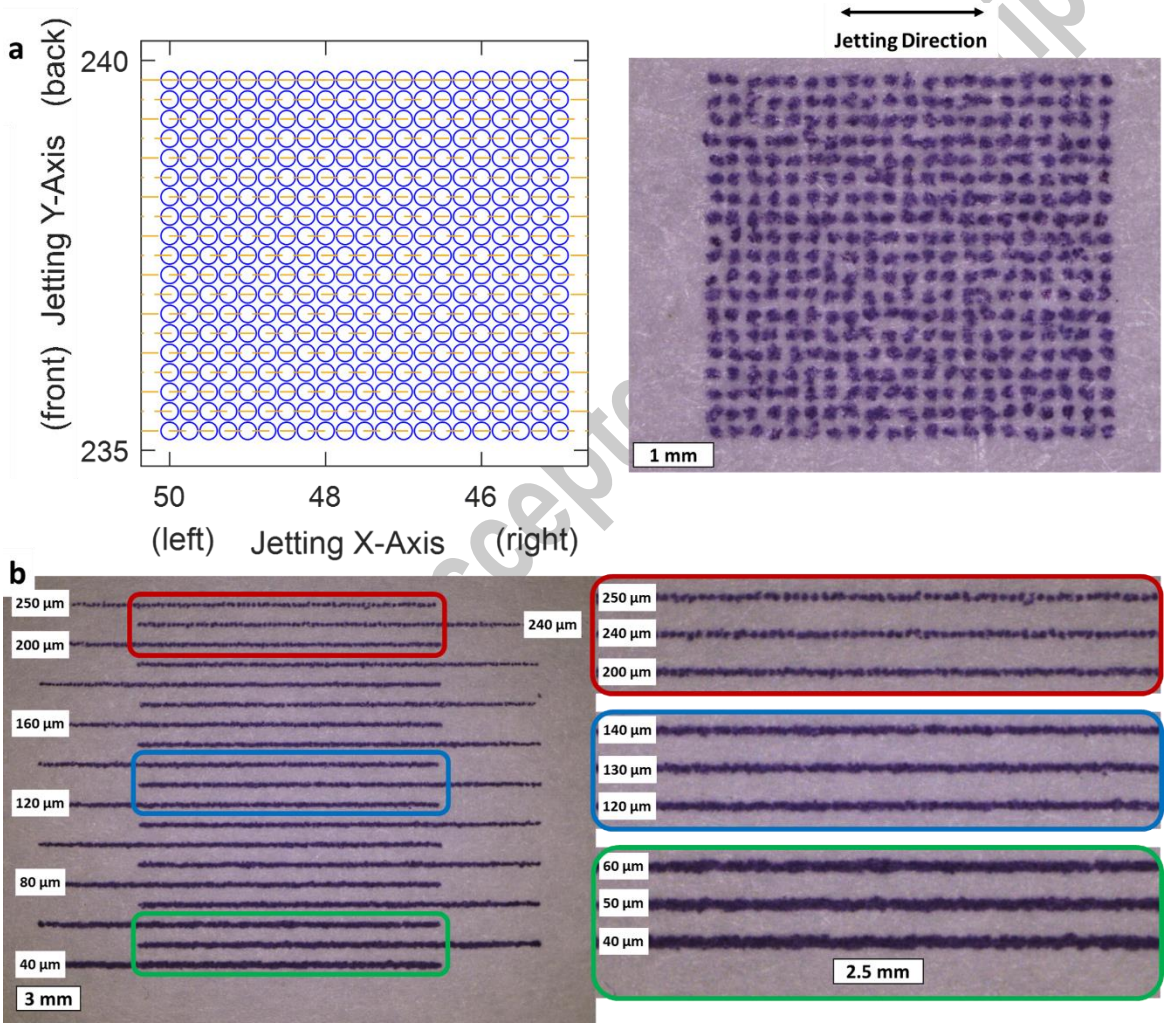

Figure 7 – (a) Droplet jetting map as created by MATLAB script and as-printed using dyed PEG binder on white paper; (b) Line formation by inkjet droplets at varying droplet spacing, with close-up of select lines, printed using dyed PEG binder on white paper.

3.2 Binder jetting experiments

To validate the utility of the full testbed, exemplary binder jetting experiments are now presented. The purpose of the following experiments is to showcase the operational capabilities of the testbed and is not intended as a full description of possible process parameter variations, nor is post-processing explored. For this validation study, a 3 mm x 5 mm x 2.5 mm rectangular prism was selected as the print geometry. Stainless steel 316L powder (15-45 µm, John Galt Steel) was spread to 100 µm layer heights using the roller mechanism at a traverse speed of 5 mm/s and a roller counter-rotation of 250 RPM. A PEG 6000 binder with 10% m/m concentration in a DI water / ethanol (20% mole fraction ethanol) solvent was deposited on the powder bed using the 80 µm nozzle dispenser, with a droplet spacing of 40 µm (0.5X droplet diameter), and a jetting traverse speed of 25 mm/s – thus controlling the binder saturation through the line spacing dimension. A base layer of 250 µm thickness was spread prior to beginning the printing process to facilitate part removal after printing. Printing was performed at 58.0 % humidity (AcuRite 01080M) in an ambient lab environment. After each layer, drying of the binder was performed by setting the heat lamp over the build area and providing power to the heat lamp for 20 seconds. After completion of the full print (i.e., printing of all 25 layers), the build platform along with the printed component and excess surrounding powder were removed. These were heated to 60°C for 30 minutes in a furnace (Pentron Laboratory Technologies, LLC JP 1200 Porcelain Furnace) to cure the binder. After binder curing, excess powder was removed from the build platform using a brush, followed by careful removal of excess powder around the part using pressurized air, and finally removal of the printed component using soft-tipped tweezers.

3.2.1 Effect of binder saturation on print quality

To study the effect of binder saturation on print quality, parts were printed with 150% and 200% estimated binder saturation. Estimated binder saturation, a process parameter for our testbed, is calculated by using the jetting parameters of droplet diameter (d), droplet spacing (D_s), line spacing (L_s) and an estimated powder bed packing fraction ($P_{f,est}$), as follows

$$S_{est} = \frac{\pi}{6} \frac{d^3}{\left(1 - P_{f,est}\right) * D_s * L_s} \quad (1)$$

An estimated powder bed packing ratio ($P_{f,est}$ = 0.5) is used in the calculation of the estimated binder saturation, since the powder bed density (equivalently, the packing fraction) is difficult to measure in-situ without disturbing the powder bed and is further locally affected by powder feedstock, spreading parameters, and environmental conditions. This value can be verified by measurement of green density after printing, and therefore can be fed back into the process parameter calculation as development proceeds. The component printed with 150% estimated binder saturation (90 µm line spacing) resulted in shifting of printed layers, shown in Figure 8. Although individual layers approach the desired area dimensions (5.02 mm x 3.05 mm), insufficient adhesion occurs between printed lines, resulting in visible individual print lines on the part. Also, the shifted layers suggest insufficient adhesion between layers also occurs, resulting in sub-optimal inter-layer strength that does not withstand the forces of spreading the next layer. The inter-line and inter-layer defects suggest the selected line spacing (and thus binder saturation) is suboptimal for this selected binder and powder combination.

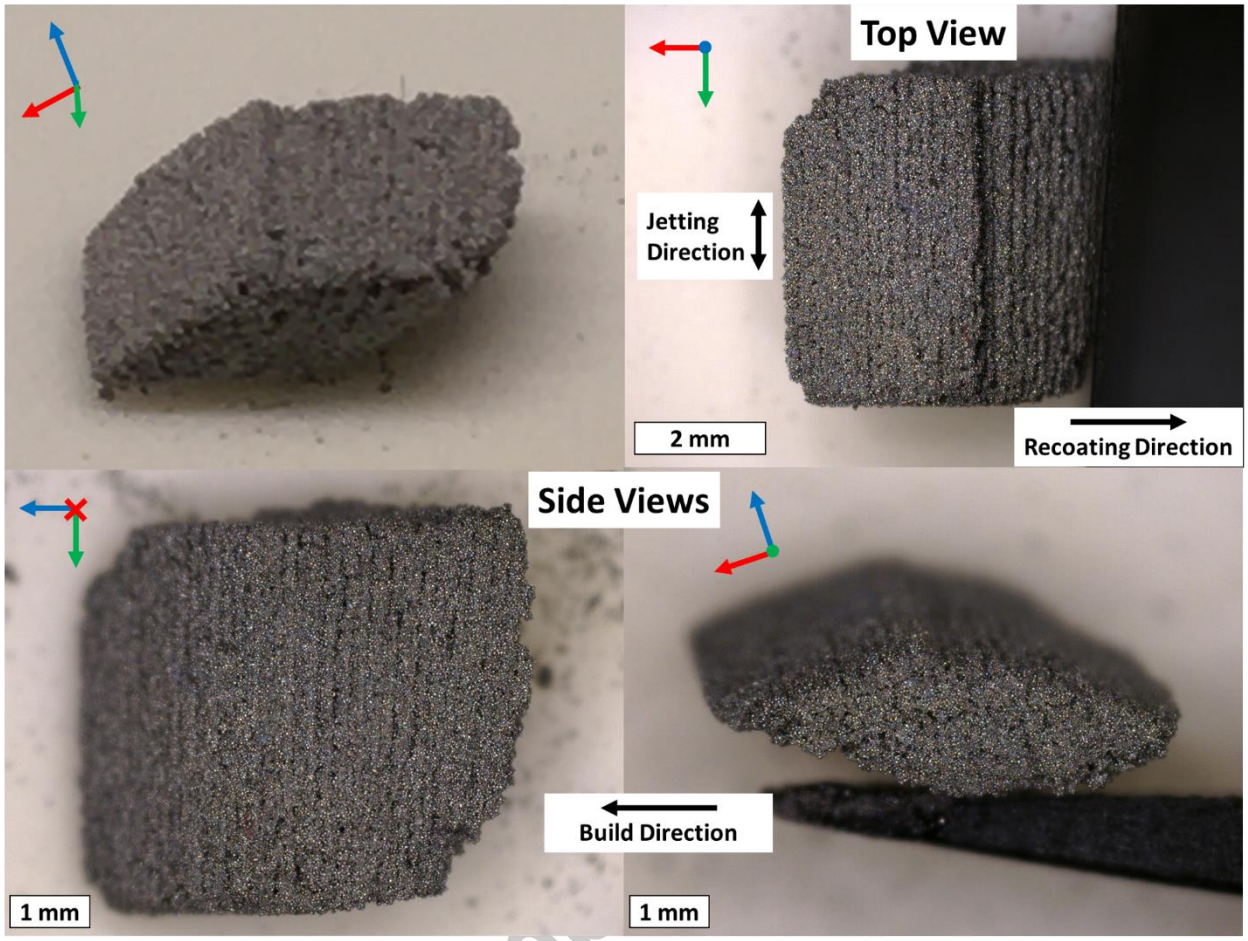

Figure 8 – Images of binder jet part (intended to be 3 mm x 5 mm x 2.5 mm right rectangular prism) printed with stainless steel 316L 15-45 µm powder with PEG binder at 150% estimated binder saturation. The result is an oblique rectangular prism due to shifted layers resultant from insufficient inter-layer binder penetration and layer shifting during powder spreading.

Alternatively, 200% estimated binder saturation (67 µm line spacing) resulted in a regular rectangular prism with dimensions of 3.09 ±0.03 mm x 5.17 ±0.02 mm x 2.51 ±0.03 mm, shown in Figure 9. For this component, individual lines are no longer visible for the top layer and no shifting occurs between layers during the print. Some defects can be seen in the side views of the component, possibly due to printing error or green part deformation through handling after printing. Additionally, the component is slightly oversized when compared to the design file, a result of excessive binder saturation at the shell regions of the print. Despite the small defects, the successful printing of the prism shows the capability of the binder jet testbed to produce relevant BJAM components utilizing custom-developed binders. Optimization of binders, printing parameters, and post-processing procedures will lead to improvements in dimensional accuracy and part strength.

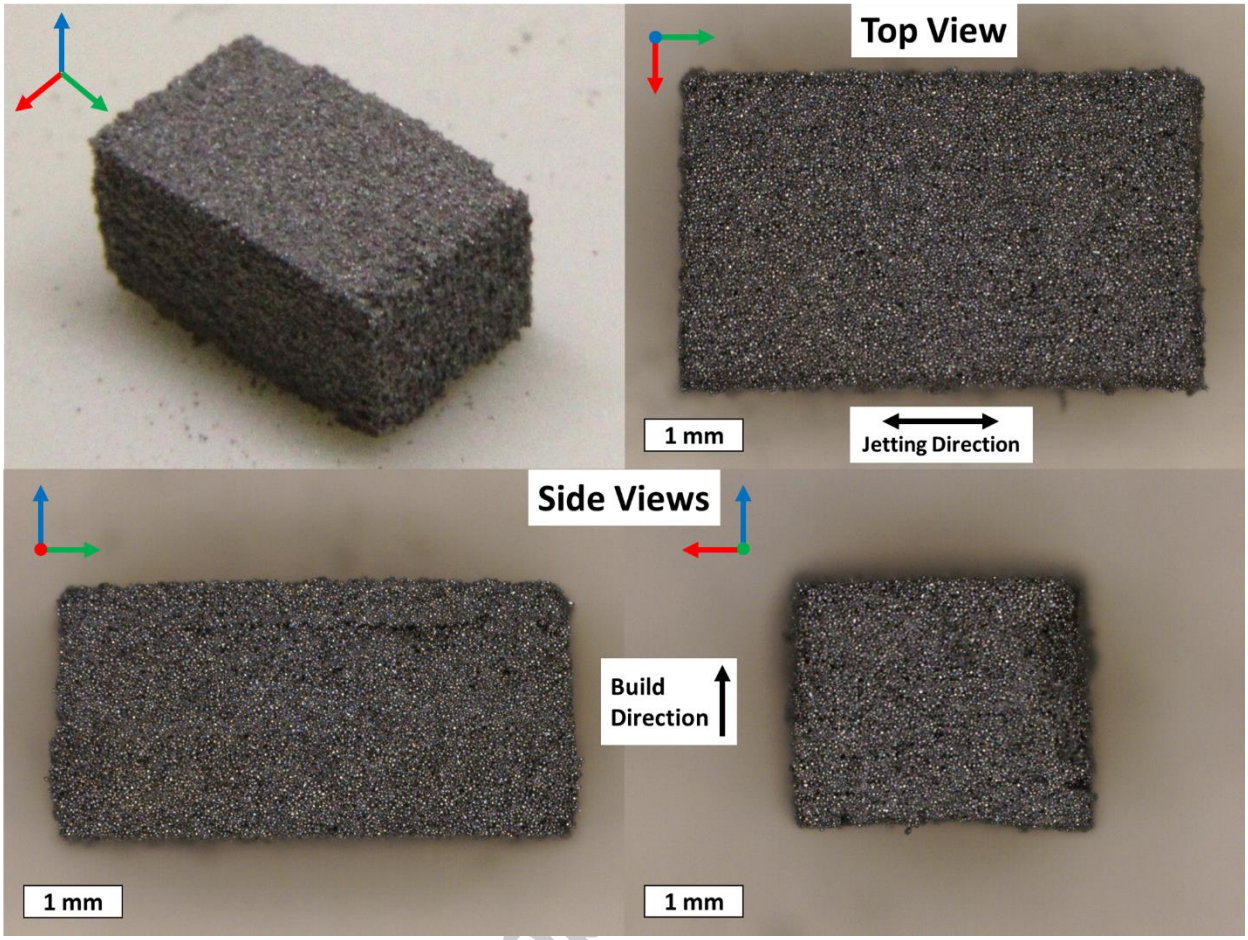

Figure 9 - Images of binder jet part (intended to be 3 mm x 5 mm x 2.5 mm right rectangular prism) printed with stainless steel 316L 15-45 µm powder with PEG binder at 200% estimated binder saturation. The result is a right rectangular prism with dimensions of 3.09 ±0.03 mm x 5.17 ±0.02 mm x 2.51 ±0.03 mm.

3.2.2 Density and µCT analysis of printed component

To further quantify the quality of the printed rectangular prism component, green density measurements were determined via micro-computed tomography (µCT), according to the parameters in Figure S1. Reconstruction was performed automatically using the control and acquisition software (Zeiss Scout-and-Scan). Fiji/ImageJ was used for image processing of the µCT 16-bit tomograms by converting to 8-bit, enhancing brightness/contrast (ImageJ auto), sharpening (ImageJ default), and thresholding (ImageJ default, IJ_IsoData) to segment the data into solid material and pores, demonstrated in Figure 10b. The processed tomograms were uploaded to Dragonfly (Object Research Systems, Inc.), which was used to estimate the density of the central region of the CT scan (1.40 mm x 1.40 mm x 1.90 mm), shown in Figure 10d. The central region was selected to avoid usage of the CT scan mask in the density calculation. The calculated green density for the component is 54.6%, in good agreement with green densities fabricated via BJAM [5–7]. Using the measured green density for the component (P_f = 0.546) instead of the estimated powder bed packing ratio ($P_{f,est}$ = 0.5), along with Equation (1), the measured binder saturation for the printed component is 220% for the selected print parameters.

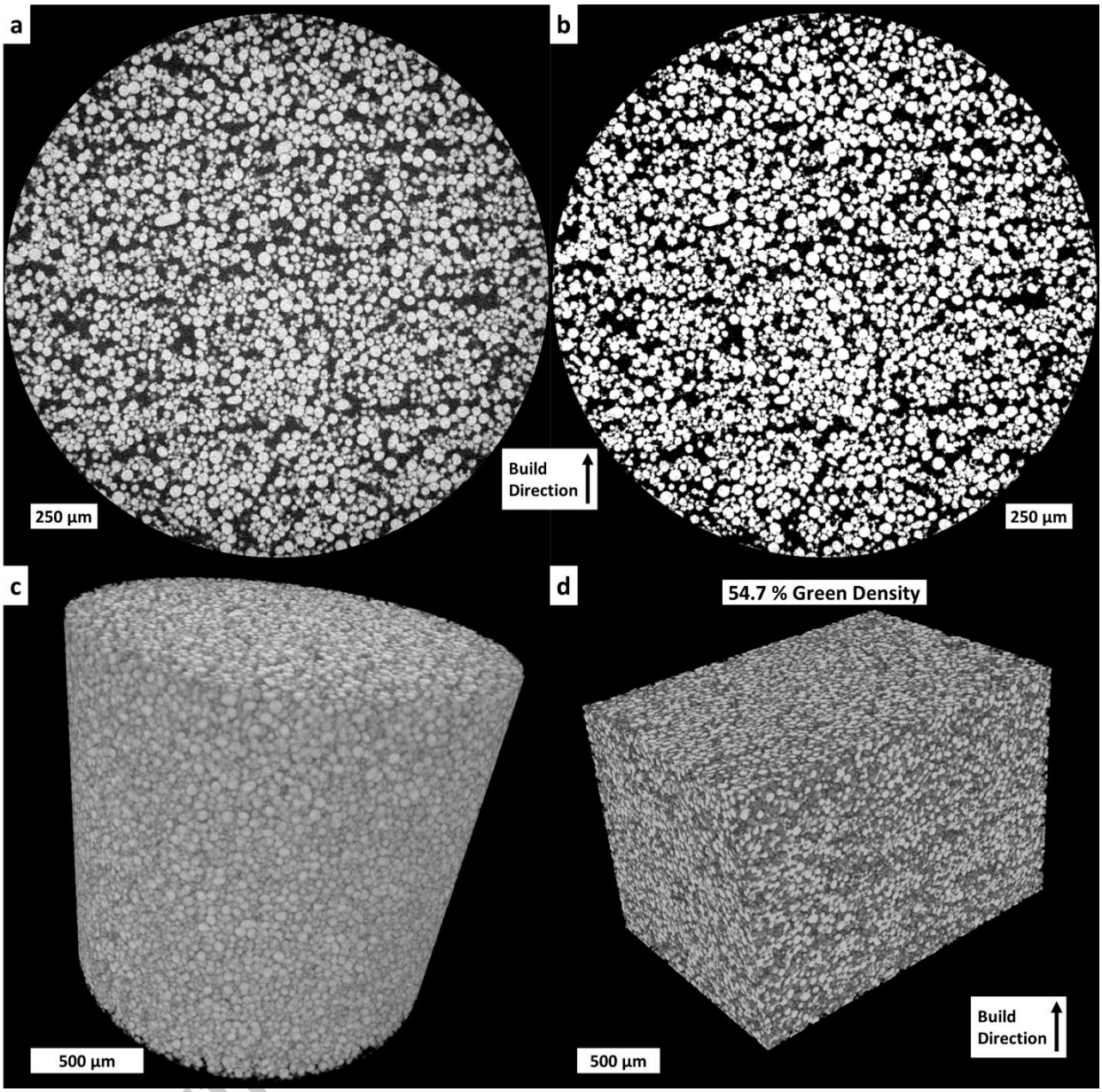

Figure 10 - µCT scan of printed part with 200% binder saturation showing: (a) exemplary tomogram from µCT scan; (b) same tomogram after contrast, sharpness, and threshold adjustment performed for density analysis; (c) 3D rendering of full µCT scan; (d) 3D rendering of µCT scan section utilized for density analysis with a calculated density of 54.6% for the green part.

4. Conclusions

This work has highlighted the design, fabrication, and validation of a modular binder jetting (BJAM) testbed. Testbed modules were validated using relevant measurement techniques, and exemplary fluid jetting and binder jetting experiments were performed to showcase the system's functionality. The system was shown to operate with commercial powder feedstocks (i.e., <50 µm D_{50} particle size), form a layer height of 100 µm, achieve inkjet droplet diameters and droplet placement fidelity <100 µm, print primitive lines on the order of 100 µm, and attain green density between 40-60% - thus comparable with

commercial research-grade binder jetting equipment. The modular design allows full authority over process parameters, as well as adaptation of spreading conditions to address powder characteristics. In particular, a single-nozzle piezoelectric inkjet dispenser, coupled with a vision system, allows identification of stable jetting parameters for arbitrary binders, and screening of jetting patterns and binder saturation levels to enable more efficient process development toward net-shape three-dimensional components. Powder spreading parameters, and incorporation of additional implements such as a dispensing hopper, could further be tailored for BJAM of fine, cohesive powders, and powders with non-spherical particle shapes. By coupling this testbed with additional characterization techniques for the powder bed, powder spreading, and powder-binder interactions, as well as post-processing capabilities (e.g., debinding and sintering), future work will explore custom binders to improve part strength and density, and study in detail the relationship between process conditions at each stage of BJAM. Research and process development using this testbed could also be translated to commercial BJAM equipment.

References

[1] M.J. Cima, E.M. Sachs, Three Dimensional Printing: Form, Materials, and Performance, Solid Free. Fabr. Symp. (1991) 187–194.

[2] E. Sachs, M. Cima, P. Williams, D. Brancazio, J. Cornie, Three dimensional printing: Rapid tooling and prototypes directly from a CAD model, J. Manuf. Sci. Eng. Trans. ASME. 114 (1992) 481–488. https://doi.org/10.1115/1.2900701.

[3] E. Sachs, M. Cima, J. Cornie, D. Brancazio, J. Bredt, A. Curodeau, T. Fan, S. Khanuja, A. Lauder, J. Lee, S. Michaels, Three-Dimensional Printing: The Physics and Implications of Additive Manufacturing, CIRP Ann. 42 (1993) 257–260. https://doi.org/10/fjxwwz.

[4] I. Gibson, D. Rosen, B. Stucker, Additive Manufacturing Technologies: 3D Printing, Rapid Prototyping, and Direct Digital Manufacturing, 2nd ed., Springer-Verlag, New York, 2015. https://doi.org/10.1007/978-1-4939-2113-3.

[5] M. Ziaee, N.B. Crane, Binder jetting: A review of process, materials, and methods, Addit. Manuf. 28 (2019) 781–801. https://doi.org/10/gf6w3x.

[6] A. Mostafaei, A.M. Elliott, J.E. Barnes, F. Li, W. Tan, C.L. Cramer, P. Nandwana, M. Chmielus, Binder jet 3D printing – Process parameters, materials, properties, and challenges, Prog. Mater. Sci. (2020) 100707. https://doi.org/10/ghjsr7.

[7] S. Mirzababaei, S. Pasebani, A Review on Binder Jet Additive Manufacturing of 316L Stainless Steel, J. Manuf. Mater. Process. 3 (2019) 82. https://doi.org/10/ghks76.

[8] M. Nastac, R. Lucas, A. Klein, Microstructure and Mechanical Properties Comparison of 316L Parts Produced by Different Additive Manufacturing Processes, Solid Free. Fabr. Symp. (2017) 10.

[9] I. Polozov, V. Sufiiarov, A. Shamshurin, Synthesis of titanium orthorhombic alloy using binder jetting additive manufacturing, Mater. Lett. 243 (2019) 88–91. https://doi.org/10/ggc6fb.

[10] A.M. Elliott, P. Nandwana, D. Siddel, B.G. Compton, A Method for Measuring Powder Bed Density in Binder Jet Additive Manufacturing Process and the Powder Feedstock Characteristics Influencing the Powder Bed Density, Solid Free. Fabr. Symp. (2016) 7.

[11] A. Mostafaei, P. Rodriguez De Vecchis, I. Nettleship, M. Chmielus, Effect of powder size distribution on densification and microstructural evolution of binder-jet 3D-printed alloy 625, Mater. Des. 162 (2019) 375–383. https://doi.org/10/ggc6fg.

[12] P. Nandwana, A.M. Elliott, D. Siddel, A. Merriman, W.H. Peter, S.S. Babu, Powder bed binder jet 3D printing of Inconel 718: Densification, microstructural evolution and challenges☆, Curr. Opin. Solid State Mater. Sci. 21 (2017) 207–218. https://doi.org/10/gc5r5n.
[13] M.T. Stawovy, K. Myers, S. Ohm, Binder jet printing of tungsten heavy alloy, Int. J. Refract. Met. Hard Mater. 83 (2019) 104981. https://doi.org/10/ghktg6.
[14] Y. Bai, C.B. Williams, An exploration of binder jetting of copper, Rapid Prototyp. J. 21 (2015) 177–185. https://doi.org/10/f68snm.
[15] T.A. Le Néel, P. Mognol, J.-Y. Hascoët, A review on additive manufacturing of sand molds by binder jetting and selective laser sintering, Rapid Prototyp. J. 24 (2018) 1325–1336. https://doi.org/10/gfktvg.
[16] M. Upadhyay, T. Sivarupan, M. El Mansori, 3D printing for rapid sand casting—A review, J. Manuf. Process. 29 (2017) 211–220. https://doi.org/10/gcgt44.
[17] J. Yoo, M.J. Cima, S. Khanuja, E.M. Sachs, Structural Ceramic Components by 3D Printing, Solid Free. Fabr. Symp. (1993) 11.
[18] E. Mendoza Jimenez, D. Ding, L. Su, A.R. Joshi, A. Singh, B. Reeja-Jayan, J. Beuth, Parametric analysis to quantify process input influence on the printed densities of binder jetted alumina ceramics, Addit. Manuf. 30 (2019) 100864. https://doi.org/10/ggnhpr.
[19] R.K. Enneti, K.C. Prough, Effect of binder saturation and powder layer thickness on the green strength of the binder jet 3D printing (BJ3DP) WC-12%Co powders, Int. J. Refract. Met. Hard Mater. 84 (2019) 104991. https://doi.org/10/ghks8x.
[20] C.L. Cramer, A.M. Elliott, J.O. Kiggans, B. Haberl, D.C. Anderson, Processing of complex-shaped collimators made via binder jet additive manufacturing of B4C and pressureless melt infiltration of Al, Mater. Des. 180 (2019) 107956. https://doi.org/10/ghks8z.
[21] W. Du, M. Singh, D. Singh, Binder jetting additive manufacturing of silicon carbide ceramics: Development of bimodal powder feedstocks by modeling and experimental methods, Ceram. Int. 46 (2020) 19701–19707. https://doi.org/10/ghktb6.
[22] M.P. Paranthaman, C.S. Shafer, A.M. Elliott, D.H. Siddel, M.A. McGuire, R.M. Springfield, J. Martin, R. Fredette, J. Ormerod, Binder Jetting: A Novel NdFeB Bonded Magnet Fabrication Process, JOM. 68 (2016) 1978–1982. https://doi.org/10/ghks87.
[23] R.M. German, Sintering Theory and Practice, Wiley, 1996.
[24] Y. Bai, G. Wagner, C.B. Williams, Effect of Particle Size Distribution on Powder Packing and Sintering in Binder Jetting Additive Manufacturing of Metals, J. Manuf. Sci. Eng. 139 (2017). https://doi.org/10/gf7wp8.
[25] M. Ziaee, E.M. Tridas, N.B. Crane, Binder-Jet Printing of Fine Stainless Steel Powder with Varied Final Density, JOM. 69 (2017) 592–596. https://doi.org/10/f9zc86.
[26] I. Rishmawi, M. Salarian, M. Vlasea, Tailoring green and sintered density of pure iron parts using binder jetting additive manufacturing, Addit. Manuf. 24 (2018) 508–520. https://doi.org/10/ggsk9v.
[27] A. Budding, T.H.J. Vaneker, New Strategies for Powder Compaction in Powder-based Rapid Prototyping Techniques, Procedia CIRP. 6 (2013) 527–532. https://doi.org/10/gf7wqj.
[28] S. Cao, Y. Qiu, X.-F. Wei, H.-H. Zhang, Experimental and theoretical investigation on ultra-thin powder layering in three dimensional printing (3DP) by a novel double-smoothing mechanism, J. Mater. Process. Technol. 220 (2015) 231–242. https://doi.org/10/f66j8x.
[29] K. Myers, A. Paterson, T. Iizuka, A. Klein, The Effect of Print Speed on Surface Roughness and Density Uniformity of Parts Produced Using Binder Jet 3D Printing, Solid Free. Fabr. Symp. (2019) 12.
[30] S.J. Gregorski, High green density metal parts by vibrational compaction of dry powder in three dimensional printing process, Thesis, Massachusetts Institute of Technology, 1996. https://dspace.mit.edu/handle/1721.1/8179 (accessed November 20, 2020).

[31] N.D. Parab, J.E. Barnes, C. Zhao, R.W. Cunningham, K. Fezzaa, A.D. Rollett, T. Sun, Real time observation of binder jetting printing process using high-speed X-ray imaging, Sci. Rep. 9 (2019) 2499. https://doi.org/10/gf7wpw.
[32] T. Colton, N.B. Crane, Influence of droplet velocity, spacing, and inter-arrival time on line formation and saturation in binder jet additive manufacturing, Addit. Manuf. (2020) 101711. https://doi.org/10/ghks9j.
[33] T. Fan, Droplet-powder impact interaction in three dimensional printing, Thesis, Massachusetts Institute of Technology, 1996. https://dspace.mit.edu/handle/1721.1/10948 (accessed November 20, 2020).
[34] R.M. German, Particle Packing Characteristics, Metal Powder Industries Federation, 1989.
[35] R.M. German, Sintering: From Empirical Observations to Scientific Principles, Butterworth-Heinemann, 2014.
[36] C. Meier, R. Weissbach, J. Weinberg, W.A. Wall, A.J. Hart, Critical influences of particle size and adhesion on the powder layer uniformity in metal additive manufacturing, J. Mater. Process. Technol. 266 (2019) 484–501. https://doi.org/10/ghktdt.
[37] S.-J.J. Lee, Powder layer generation for three dimensional printing, Thesis, Massachusetts Institute of Technology, 1992. https://dspace.mit.edu/handle/1721.1/12452 (accessed December 29, 2020).
[38] S. Barui, H. Ding, Z. Wang, H. Zhao, S. Marathe, W. Mirihanage, B. Basu, B. Derby, Probing Ink–Powder Interactions during 3D Binder Jet Printing Using Time-Resolved X-ray Imaging, ACS Appl. Mater. Interfaces. 12 (2020) 34254–34264. https://doi.org/10/ghqqn2.
[39] Y. Bai, C. Wall, H. Pham, A. Esker, C.B. Williams, Characterizing Binder–Powder Interaction in Binder Jetting Additive Manufacturing Via Sessile Drop Goniometry, J. Manuf. Sci. Eng. 141 (2018). https://doi.org/10/gf7wpv.
[40] J.F. Bredt, Binder stability and powder/binder interaction in three dimensional printing, Thesis, Massachusetts Institute of Technology, 1995. https://dspace.mit.edu/handle/1721.1/10999 (accessed December 29, 2020).
[41] M. Esterman, Characterization of the powder/binder interaction in the three dimensional printing process, Thesis, Massachusetts Institute of Technology, 1990. https://dspace.mit.edu/handle/1721.1/13671 (accessed December 29, 2020).
[42] R.K. Holman, M.J. Cima, S.A. Uhland, E. Sachs, Spreading and Infiltration of Inkjet-Printed Polymer Solution Droplets on a Porous Substrate, J. Colloid Interface Sci. 249 (2002) 432–440. https://doi.org/10/btch83.
[43] B. Utela, D. Storti, R. Anderson, M. Ganter, A review of process development steps for new material systems in three dimensional printing (3DP), J. Manuf. Process. 10 (2008) 96–104. https://doi.org/10/fhcbqw.
[44] B.R. Utela, D. Storti, R.L. Anderson, M. Ganter, Development Process for Custom Three-Dimensional Printing (3DP) Material Systems, J. Manuf. Sci. Eng. 132 (2010). https://doi.org/10/cv4xhb.
[45] J. Moon, J.E. Grau, V. Knezevic, M.J. Cima, E.M. Sachs, Ink-Jet Printing of Binders for Ceramic Components, J. Am. Ceram. Soc. 85 (2002) 755–762. https://doi.org/10/cngrvn.
[46] L.O. Grant, M.B. Alameen, J.R. Carazzone, C.F.H. Iii, Z.C. Cordero, Mitigating Distortion During Sintering of Binder Jet Printed Ceramics, Solid Free. Fabr. Symp. (2018) 8.
[47] Y. Bai, C.B. Williams, Binderless Jetting: Additive Manufacturing of metal parts via jetting nanoparticles, Solid Free. Fabr. Symp. (2017) 12.
[48] R.M. German, Theory of thermal debinding, Int J Powder Met. 23 (1987) 237–245.
[49] R.K. Enneti, S.J. Park, R.M. German, S.V. Atre, Review: Thermal Debinding Process in Particulate Materials Processing, Mater. Manuf. Process. 27 (2012) 103–118. https://doi.org/10/drpr72.
[50] Y. Bai, C.B. Williams, Binder jetting additive manufacturing with a particle-free metal ink as a binder precursor, Mater. Des. 147 (2018) 146–156. https://doi.org/10/gdc3rb.

[51] Y. Bai, C.B. Williams, The effect of inkjetted nanoparticles on metal part properties in binder jetting additive manufacturing, Nanotechnology. 29 (2018) 395706. https://doi.org/10/ghks9f.
[52] A. Elliott, S. AlSalihi, A.L. Merriman, M.M. Basti, Infiltration of Nanoparticles into Porous Binder Jet Printed Parts, Am. J. Eng. Appl. Sci. 9 (2016). https://doi.org/10/ghks9g.
[53] P. Torabi, M. Petros, B. Khoshnevis, Selective Inhibition Sintering: The Process for Consumer Metal Additive Manufacturing, 3D Print. Addit. Manuf. 1 (2014) 152–155. https://doi.org/10/ghks9c.
[54] H.J. Yoo, Reactive binders for metal parts produced by Three Dimensional Printing, Thesis, Massachusetts Institute of Technology, 1997. https://dspace.mit.edu/handle/1721.1/32315 (accessed November 20, 2020).
[55] E.M. Sachs, C. Hadjiloucas, S. Allen, H.J. Yoo, Metal and ceramic containing parts produced from powder using binders derived from salt, US6508980B1, 2003. https://patents.google.com/patent/US6508980B1/en (accessed November 20, 2020).
[56] N.B. Crane, J. Wilkes, E. Sachs, S.M. Allen, Improving accuracy of powder-based SFF processes by metal deposition from a nanoparticle dispersion, Rapid Prototyp. J. 12 (2006) 266–274. https://doi.org/10/fmtmsh.
[57] M.L. Vlasea, B.M. Lane, F.F. Lopez, S. Mekhontsev, M.A. Donmez, Development of powder bed fusion additive manufacturing test bed for enhanced real time process control, Solid Free. Fabr. Symp. (2015) 527–539.
[58] P. Bidare, R.R.J. Maier, R.J. Beck, J.D. Shephard, A.J. Moore, An open-architecture metal powder bed fusion system for in-situ process measurements, Addit. Manuf. 16 (2017) 177–185. https://doi.org/10/ggbqkj.
[59] B. N. Turner, R. Strong, S. A. Gold, A review of melt extrusion additive manufacturing processes: I. Process design and modeling, Rapid Prototyp. J. 20 (2014) 192–204. https://doi.org/10/f6fhmc.
[60] B.N. Turner, S.A. Gold, A review of melt extrusion additive manufacturing processes: II. Materials, dimensional accuracy, and surface roughness, Rapid Prototyp. J. 21 (2015) 250–261. https://doi.org/10/f7czst.
[61] S. Vock, B. Klöden, A. Kirchner, T. Weißgärber, B. Kieback, Powders for powder bed fusion: a review, Prog. Addit. Manuf. 4 (2019) 383–397. https://doi.org/10/gg7r92.
[62] W.E. King, A.T. Anderson, R.M. Ferencz, N.E. Hodge, C. Kamath, S.A. Khairallah, A.M. Rubenchik, Laser powder bed fusion additive manufacturing of metals; physics, computational, and materials challenges, Appl. Phys. Rev. 2 (2015) 041304. https://doi.org/10/gf3jwx.
[63] C.Y. Yap, C.K. Chua, Z.L. Dong, Z.H. Liu, D.Q. Zhang, L.E. Loh, S.L. Sing, Review of selective laser melting: Materials and applications, Appl. Phys. Rev. 2 (2015) 041101. https://doi.org/10/gctr3t.
[64] T. Wohlers, I. Campbell, O. Diegel, R. Huff, J. Kowen, Wohlers Report 2020: 3D Printing and Additive Manufacturing Global State of the Industry, Wohlers Associates, Inc, 2020.
[65] L.I. Escano, N.D. Parab, L. Xiong, Q. Guo, C. Zhao, K. Fezzaa, W. Everhart, T. Sun, L. Chen, Revealing particle-scale powder spreading dynamics in powder-bed-based additive manufacturing process by high-speed x-ray imaging, Sci. Rep. 8 (2018) 15079. https://doi.org/10/gfgfn9.
[66] Z. Snow, R. Martukanitz, S. Joshi, On the development of powder spreadability metrics and feedstock requirements for powder bed fusion additive manufacturing, Addit. Manuf. 28 (2019) 78–86. https://doi.org/10/ghq4ss.
[67] D. Gilmer, L. Han, E. Hong, D. Siddel, A. Kisliuk, S. Cheng, D. Brunermer, A. Elliott, T. Saito, An in-situ crosslinking binder for binder jet additive manufacturing, Addit. Manuf. 35 (2020). https://doi.org/10/ghktcj.
[68] H. Zhao, C. Ye, S. Xiong, Z. Fan, L. Zhao, Fabricating an effective calcium zirconate layer over the calcia grains via binder-jet 3D-printing for improving the properties of calcia ceramic cores, Addit. Manuf. 32 (2020) 101025. https://doi.org/10/ghktcn.

[69] ExOne, Innovent+®, (n.d.). https://www.exone.com/en-US/3D-printing-systems/metal-3d-printers/Innovent (accessed November 20, 2020).
[70] D.S. Uduwage, Binder Jet Additive Manufacturing of Stainless Steel-Hydroxyapatite Bio-composite, Grad. Theses Diss. Capstone Proj. (2015). https://cornerstone.lib.mnsu.edu/etds/432.
[71] B. Derby, Inkjet Printing of Functional and Structural Materials: Fluid Property Requirements, Feature Stability, and Resolution, Annu. Rev. Mater. Res. 40 (2010) 395–414. https://doi.org/10/dppfm2.
[72] S. Magdassi, The Chemistry Of Inkjet Inks, World Scientific, 2009.
[73] I.M. Hutchings, G.D. Martin, Inkjet Technology for Digital Fabrication, 1st ed., John Wiley & Sons, Ltd, 2013. https://doi.org/10.1002/9781118452943.
[74] D. Oropeza, R. Roberts, A.J. Hart, A modular testbed for mechanized spreading of powder layers for additive manufacturing, Rev. Sci. Instrum. 92 (2021) 015114. https://doi.org/10/ghszgr.
[75] R.M. German, A. Bose, Binder and Polymer Assisted Powder Processing, ASM International, 2020.

Graphical Abstract: